

# Mechanistic insights into marine boundary layer nucleation: synergistic interactions of typical sulfur, iodine, and nitrogen precursors

Jing Li<sup>1</sup>, An Ning<sup>1,\*</sup>, Ling Liu<sup>1</sup>, Xiucong Deng<sup>1</sup>, and Xiuhui Zhang<sup>1,\*</sup>

5 <sup>1</sup>State Key Laboratory of Environment Characteristics and Effects for Near-space, Key Laboratory of Cluster Science, Ministry of Education of China, School of Chemistry and Chemical Engineering, Beijing Institute of Technology, Beijing, 100081, China

*Correspondence to:* A. Ning (anning@bit.edu.cn) and X. H. Zhang (zhangxiuhui@bit.edu.cn)

**Abstract.** Marine new particles significantly impact the global atmosphere, yet the key nucleation process underlying their  
10 formation remains unclear. Sulfur-, nitrogen-, and iodine-containing species are expected to coexist in the marine atmosphere, including the canonical precursors methanesulfonic acid (MSA), iodic acid (IA), and dimethylamine (DMA). To elucidate how they interact to drive NPF, we performed high-level quantum chemical calculations and cluster dynamics simulations to investigate their synergistic nucleation mechanism at the molecular level. The results show that IA, MSA, and DMA form  
15 stable pre-nucleation clusters via intermolecular hydrogen and halogen bonding, with acid-base reactions during clustering, forming ion pairs. The proposed IA–MSA–DMA ternary nucleation is thermodynamically more favorable in regions rich in sulfur and nitrogen but poor in iodine. Its cluster formation rate is notably higher than that of any corresponding binary nucleation, showing a synergistic enhancement of 4–8 orders of magnitude. Moreover, this rate even exceeds that of the well-established efficient iodine oxoacids nucleation under sulfur-rich conditions. In polar coastal regions such as Aboa and  
20 Marambio, the inclusion of the IA–MSA–DMA nucleation pathway brings simulated nucleation rates closer to field measurements than considering the established IA–DMA nucleation alone, identifying it as a critical mechanism in these environments. Accordingly, the proposed IA–MSA–DMA nucleation mechanism is expected to be important in the marine boundary layer, helping to explain the missing sources of marine particles, especially in cold polar marine regions. Incorporating this mechanism into atmospheric modelling can potentially improve aerosol formation simulations and refine climate predictions.

## 25 1 Introduction

Marine aerosols represent the largest aerosol system on Earth, influencing global radiative balance and climate change (O'Dowd and Leeuw, 2007; Zhang et al., 2012). Notably, aerosols are the primary source of uncertainty in climate forcing (Gettelman and Kahn, 2025). Aerosols originate primarily from new particle formation (NPF), initiated by nucleation processes that involves the gas-to-particle transition—a critical yet elusive stage (Kulmala et al., 2013). Field studies have shown that

30 marine NPF events are closely linked to iodine-bearing precursors, with iodic acid ( $\text{HIO}_3$ , IA) playing a key role in driving nucleation (Sipilä et al., 2016; Baccharini et al., 2020; Beck et al., 2021; He et al., 2021; He et al., 2023).

Although IA is abundant and widespread, its self-nucleation is insufficient to explain the fast nucleation observed (Ning et al., 2022a; Ma et al., 2023). Even with the effective stabilization by iodous acid ( $\text{HIO}_2$ ), the predicted nucleation rates cannot fully account for the high values measured in previous experiments (Engsvang and Elm, 2025). As an acidic precursor, IA is readily stabilized by atmospheric base such as ammonia ( $\text{NH}_3$ ) and amines (e.g., dimethylamine, DMA) (Rong et al., 2020; Xia et al., 2020; Ning et al., 2022b; Ma et al., 2023; Li et al., 2024) via acid-base reactions. Among these bases, DMA stabilizes IA more efficiently—by 1000-fold compared to  $\text{NH}_3$  (Ning et al., 2022b). Accordingly, when  $\text{NH}_3$  and DMA coexist, IA–DMA clusters play a more important role in nucleation under ambient conditions of boundary layer (Li et al., 2024). A recent study has also confirmed that IA–amine nucleation is efficient enough to be comparable to the well-established sulfuric acid–amine nucleation, provided that IA exceeds sulfuric acid by a factor of 10 (Engsvang and Elm, 2025). However, IA–DMA mechanism overlooks the roles and effects of other effective nucleation precursors, failing to capture the complexity of real atmospheric scenarios.

Alongside the aforementioned efficient iodine (IA) and nitrogen (DMA) precursors, historically, sulfur-containing compounds have also been regarded as vital nucleation agents over oceans, primarily the oxidation product of dimethyl sulfide (DMS) (Hodshire et al., 2019; Hoffmann et al., 2016). As the typical oxidation product of DMS, methanesulfonic acid (MSA) is ubiquitous in marine atmospheres, often present at considerable concentrations (Chen et al., 2018; Dal Maso et al., 2002; Yan et al., 2019; Eisele and Tanner, 1993), and existing observational data may even underestimate its true levels (Yan et al., 2019). More importantly, MSA shows effective nucleation potential, even comparable to that of  $\text{H}_2\text{SO}_4$  (Liu et al., 2022; Perraud et al., 2015; Dawson et al., 2012), and can individually bind with IA and DMA to form binary clusters, respectively (Ning et al., 2022a; Chen et al., 2016; Chen and Finlayson-Pitts, 2017). Nevertheless, theoretical studies suggest that electrically neutral clusters consisting solely of MSA (as the clustering acid) are unlikely to form and grow under realistic atmospheric conditions (Elm, 2021). Moreover, field observations indicate that MSA frequently coexists with IA and DMA in the marine atmosphere, and all three species are simultaneously detected in aerosol particle (Salignat et al., 2024). Collectively, the evidence points to the coexistence and potential interactions of these typical marine sulfur-(MSA), iodine-(IA), and nitrogen-(DMA) precursors, implying their possibility to jointly participate in particle nucleation. However, whether these three precursors exhibit synergistic effects, as well as the underlying molecular mechanisms and their atmospheric implications, remains unclear. Thus, elucidating the IA–MSA–DMA ternary nucleation process is crucial for a deeper understanding of the underlying origins of marine NPF events.

Herein, we investigated the IA–MSA–DMA ternary nucleation system (denoted as  $(\text{IA})_x(\text{MSA})_y(\text{DMA})_z$ , where  $x + y + z \leq 6$  and  $x + y \geq z$ ) at the molecular level using quantum chemical (QC) calculations and cluster dynamics simulations. QC calculations and wavefunction analyses were performed to clarify the physicochemical nature of clustering, while nucleation rates under varying atmospheric conditions were calculated to reveal nucleation dynamics. By comparing nucleation simulations with field observations (or other well-established nucleation systems), we assess and quantify the importance of

IA–MSA–DMA nucleation mechanism. Furthermore, by analyzing the nucleation pathway under different marine conditions,  
 65 we quantify the contribution of IA–MSA–DMA ternary nucleation to particle formation.

## 2 Methods

### 2.1 Quantum Chemistry Calculations

In this study, a multistep conformation search was employed to identify the lowest-energy structures of  $(IA)_x(MSA)_y(DMA)_z$   
 (1 ≤ x + y + z ≤ 6, x + y ≥ z) clusters. We considered only clusters in which the number of acid molecules equal to or greater  
 70 than that of base molecules, as prior computational and experimental studies indicate that clusters with excess base are  
 generally thermodynamically less stable and inefficient for nucleation under atmospherically relevant conditions (Myllys et  
 al., 2019; Ning et al., 2022b). A detailed description of the methodology is provided in the Supporting Information (SI). The  
 initial structures of pure IA clusters, as well as binary IA–MSA, IA–DMA, and MSA–DMA clusters, were adopted from the  
 previous studies (Rong et al., 2020; Ning et al., 2022a; Ning et al., 2022b; Ning and Zhang, 2022). All lowest-energy structures  
 75 of IA–MSA–DMA ternary cluster were further optimized using the Gaussian 09 program (Frisch et al., 2009) at the  $\omega$ B97X-  
 D/6-311++G(3df,3pd) (for C, H, O, N, and S atoms) + aug-cc-pVTZ-PP (for I atom) level of theory (Francl et al., 1982;  
 Peterson et al., 2003). Subsequent single-point energy calculations were carried out using the ORCA 5.0 software (Neese,  
 2012) at the DLPNO-CCSD(T)/aug-cc-pVTZ (for C, H, O, N, and S atoms) + aug-cc-pVTZ-PP (for I atom) level of theory,  
 with the TightPNO and TightSCF criteria applied to ensure high-accuracy electronic energies. Given the significant impact of  
 80 spin-orbit coupling (SOC) on energy calculations for heavy elements like iodine (Verstraete et al., 2008; Mohd Zaki et al.,  
 2023; Engsvang et al., 2024), we quantitatively evaluated SOC effects using the Gaussian 16 program (Frisch et al., 2016) at  
 the  $\omega$ B97X-D/6-311++G(3df,3pd) (for C, H, O, N, and S atoms) + dhf-TZVP-2c (for I atom) level of theory (Chan and Yim,  
 2013; Kuhn and Weigend, 2015; Sarr et al., 2021; Holzer et al., 2022). Gibbs free energies ( $\Delta G_{\text{ref}}$ , kcal mol<sup>-1</sup>) of the IA–MSA–  
 DMA clusters under standard pressure were calculated using Eq. (1):

$$85 \quad \Delta G_{\text{ref}} = \Delta G_{\text{thermal}}^{\omega\text{B97X-D}} + \Delta E_{\text{DLPNO-CCSD(T)}} + \Delta E_{\text{SOC}}, \quad (1)$$

where  $\Delta G_{\text{thermal}}^{\omega\text{B97X-D}}$  and  $\Delta E_{\text{DLPNO-CCSD(T)}}$  represent the thermal and electronic contributions to the Gibbs free energy, respectively.  
 $\Delta E_{\text{SOC}}$  denotes the relativistic correction from SOC for iodine-containing clusters. Thermal corrections ( $\Delta G_{\text{thermal}}^{\omega\text{B97X-D}}$ ) across the  
 temperature range of 258 – 298 K were obtained using Shermo 2.0 software (Lu and Chen, 2021). Final Gibbs free energies  
 are summarized in Table S1 of the SI. To account for the influence of precursor concentrations, the  $\Delta G_{\text{ref}}$  was further converted  
 90 to the concentration-dependent Gibbs free energy ( $\Delta G$ ) using Eq. (2):

$$\Delta G(P_1, P_2, \dots, P_n) = \Delta G_{\text{ref}} - k_{\text{B}}T \sum_{i=1}^n N_i \ln \left( \frac{P_i}{P_{\text{ref}}} \right), \quad (2)$$

where  $P_{\text{ref}}$  is the reference pressure (1 atm),  $k_{\text{B}}$  is the Boltzman constant,  $T$  is the temperature,  $N_i$  is the number of molecules  $i$  in the cluster, and  $P_i$  is the partial pressure of vapor  $i$ .

In this study, the conducted ACDC simulations accounted for all feasible collision and evaporation processes. These  
95 included interactions between monomer-monomer, monomer-cluster, and cluster-cluster pairs, in addition to the fragmentation  
of parent clusters into monomers or into two smaller clusters. Furthermore, in our ACDC simulations, the largest clusters  
considered consist of six molecules ( $\sim 1.2$  nm), which falls within the reported atmospheric nucleation critical cluster sizes of  
1.1–1.9 nm (Kulmala et al., 2013). The current system size is large enough because the largest cluster included is stable, with  
its collisions dominating evaporation. While a limited system size can, in principle, lead to a modest overestimation of the  
100 nucleation rate, computational studies indicate that expanding the scheme (e.g., from  $3 \times 3$  to  $4 \times 4$ ) yields only a minor change  
in the particle formation rate (Kubečka et al., 2023). This suggests that the cluster size employed here is sufficient for capturing  
the relevant nucleation behaviour; therefore, the present results are consequently reasonable.

## 2.2 Wavefunction Analysis

The stability of clusters is largely determined by intermolecular forces between constituent molecules. To gain deeper insight  
105 into these interactions within the IA–MSA–DMA clusters, wavefunction-based analyses were performed using the Multiwfn  
3.7 program (Lu and Chen, 2012). Specifically, the electrostatic potential (ESP) was projected onto the molecular van der  
Waals (vdW) surface to identify favorable interaction regions of the nucleating species, namely IA, MSA, and DMA.

## 2.3 Atmospheric Clusters Dynamic Simulations

The atmospheric cluster dynamic code (ACDC) (McGrath et al., 2012) was utilized to explore the cluster formation rates,  
110 growth pathways, and steady-state concentrations of the IA–MSA–DMA system by solving the birth-death equation (see the  
SI for details).

In the ACDC simulation, an enhancement factor of 2.3 was applied to the collision rate coefficient ( $\beta_{i,j}$ ) to account for  
enhanced intermolecular vdW forces (Halonen et al., 2019), consistent with its validated application in previous nucleation  
studies (Stolzenburg et al., 2020; Cai et al., 2021; Li et al., 2023; Ning et al., 2024). Additionally, the coagulation sink ( $S_i$ )  
115 (Lehtipalo et al., 2016), which varies with cluster size, was calculated using Eq. (3):

$$S_i = \text{CS}_{\text{ref}} \times (d_i / d_{\text{ref}})^{-m}, \quad (3)$$

where  $\text{CS}_{\text{ref}}$  is the condensation sink (CS) of the reference monomer (*i.e.*, IA monomer), and  $d$  denotes the diameter of either  
the monomer or the cluster. The exponent  $m$ , set to 1.7, is dependent on the background aerosol distribution and falls within  
the typical range reported for atmospheric particles (Lehtinen et al., 2007). A cluster was defined as stable when the product  
120 of its collision rate coefficient and concentration ( $\beta \cdot C$ ) surpasses the sum of its evaporation rate constants ( $\Sigma \gamma$ , Table S2). Such  
stable clusters were assumed to grow outside the simulated box without evaporating back into the system, and this criterion  
was applied to set the simulation boundary conditions (detailed in Table S3).

125 The condition settings for the ACDC simulations were based on data from field measurements, Cosmics Leaving Outdoor Droplets (CLOUD) experiments, and atmospheric modelling. For the marine boundary layer (MBL), the temperature ( $T$ ) was primarily set within the range of 258 – 298 K (Almeida et al., 2013), and the CS was set as  $2.0 \times 10^{-3} \text{ s}^{-1}$  (He et al., 2021). The concentration range of precursors was specified as:  $[\text{IA}] = 10^6 - 10^8 \text{ molec. cm}^{-3}$  (Sipilä et al., 2016),  $[\text{MSA}] = 10^6 - 10^8 \text{ molec. cm}^{-3}$  (Berresheim et al., 2002; Chen et al., 2018), and  $[\text{DMA}] = 0.025 - 2.5 \text{ pptv}$  (Yu and Luo, 2014), respectively.

## 3 Results and Discussion

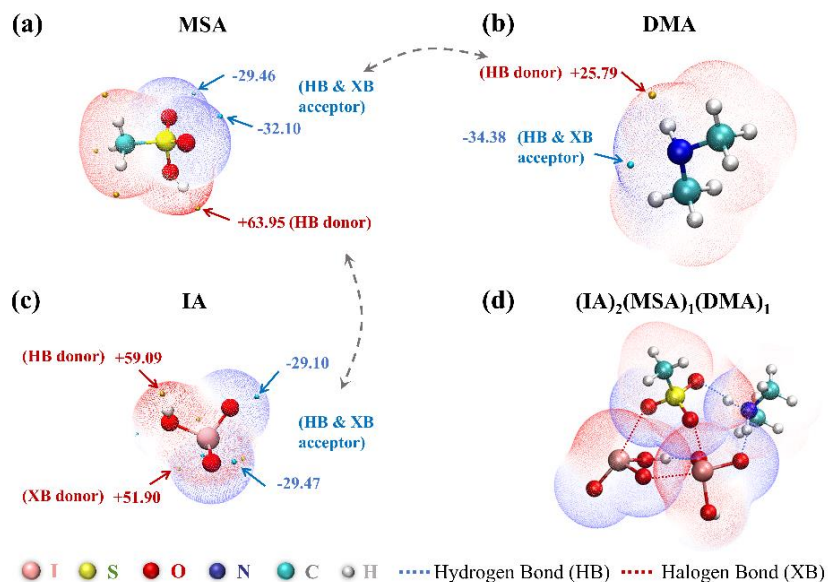
### 3.1 Cluster Structure

130 Strong intermolecular noncovalent interactions are critical in governing the formation and stability of molecular clusters. To assess the synergistic nucleation potential of IA, MSA, and DMA, the surface electrostatic potential (ESP) mapped on van der Waals (vdW) surfaces of these molecules was analyzed using the Multiwfn 3.7 (Lu and Chen, 2012), based on the calculated wavefunctions at the  $\omega\text{B97X-D/6-311++G(3df,3pd)}$  (for C, H, O, N, and S atoms) + aug-cc-pVTZ-PP (for I atom) level of theory. The resulting ESP maps are presented in Fig. 1, where regions of positive and negative potential are depicted in red and blue, respectively. A positive ESP indicates an electrophilic region, suggesting a propensity to function as a donor in hydrogen bond (HB) or halogen bond (XB) interactions. In contrast, a negative ESP denotes a nucleophilic region, which is likely to serve as an acceptor in HB or XB interactions. A more detailed analysis is provided in the SI. ESP analysis demonstrates the potential for intermolecular interactions among IA, MSA, and DMA, thereby leading to further clustering.

140 To structurally elucidate the physicochemical nature of clustering, conformational analysis was performed to reveal the characters of intermolecular interactions within the identified ternary IA–MSA–DMA clusters (Fig. S1), where the red and black dashed lines denote XBs and HBs, respectively. The Cartesian coordinates of the optimized cluster structures are listed in Table S4. Overall, the resulting IA–MSA–DMA clusters are stabilized by a network of HBs and XBs. HBs are the most prevalent interaction type, constituting  $\sim 74\%$  of all identified non-covalent interactions across all optimized ternary IA–MSA–DMA clusters. Two types of HBs ( $\text{N-H}\cdots\text{O}$  and  $\text{O-H}\cdots\text{O}$ ) are observed, with  $\text{N-H}\cdots\text{O}$  HBs dominating (71%) among the total HB interactions identified and typically forming between acids (IA and MSA) and base (DMA). On the contrary, in the binary IA–DMA system,  $\text{N-H}\cdots\text{O}$  HBs represent a slightly lower proportion ( $\sim 60\%$ ) and are exclusively formed between IA and DMA. Additionally, both MSA and DMA has methyl groups ( $-\text{CH}_3$ ) that are generally located on the periphery of IA–MSA–DMA clusters. This spatial arrangement facilitates the formation of HBs and XBs, reducing steric hindrance, promoting clustering, and enhancing stability.

150 During cluster formation, acid-base reactions between acid molecules (IA and MSA) and the base molecule (DMA) often occur, resulting in proton transfer and the formation of ion pairs such as  $\text{IO}_3^- - \text{DMAH}^+$  and  $\text{CH}_3\text{SO}_3^- - \text{DMAH}^+$ . Another distinct feature compared to the binary IA–DMA pathway is the preferential protonation of DMA by the stronger acid MSA ( $\text{pK}_a = -1.9$  vs.  $0.8$  for IA), leading to a dominant  $\text{CH}_3\text{SO}_3^- - \text{DMAH}^+$  ion pair in the ternary system. This provides a different anionic center ( $\text{CH}_3\text{SO}_3^-$ ) for interaction compared to the  $\text{IO}_3^- - \text{DMAH}^+$  pair within the binary IA–DMA system. This acid-base

155 interaction not only strengthens the cluster via enhanced electrostatic stabilization but also introduces additional interaction sites for noncovalent bonding. As shown in Fig. S2, numerous unoccupied HB and XB sites are present in  $(IA)_3(MSA)_1(DMA)_2$  cluster, which can further promote the condensation of atmospheric precursors and the growth of the cluster. These results indicate that IA, MSA, and DMA can form molecular clusters stabilized by a network of HBs and XBs, accompanied by acid-base reactions that produce ion pairs.



160

**Figure 1.** The ESP-mapped molecular vdW surface of (a) MSA, (b) DMA, (c) IA, and (d)  $(IA)_2(MSA)_1(DMA)_1$  cluster at the  $\omega B97X-D/6-311++G(3df,3pd)$  (for C, H, O, N, and S atoms) + aug-cc-pVTZ-PP (for I atom) level of theory. The golden and cyan dots represent the positions of maximums and minimums of ESP values (unit: kcal mol<sup>-1</sup>), respectively. The gray dashed arrows signify the site-to-site interaction tendencies.

### 165 3.2 Cluster Stability

To evaluate the thermodynamic stability of the IA–MSA–DMA clusters, concentration-dependent Gibbs free energies ( $\Delta G$ , Eq. (2)) were calculated, and free-energy profiles of the IA–MSA–DMA (ternary) and IA–DMA (binary) pathways were compared under varying precursor concentrations (Fig. 2). Overall, cluster formation energy barriers decrease with increasing precursor concentrations. The key distinction between the IA–MSA–DMA ternary and IA–DMA binary pathway arises in the step where the  $(IA)_2(DMA)_1$  cluster grows into either a  $(IA)_3(DMA)_1$  or a  $(IA)_2(MSA)_1(DMA)_1$  cluster. Thus, our discussion focuses on this critical step.

170

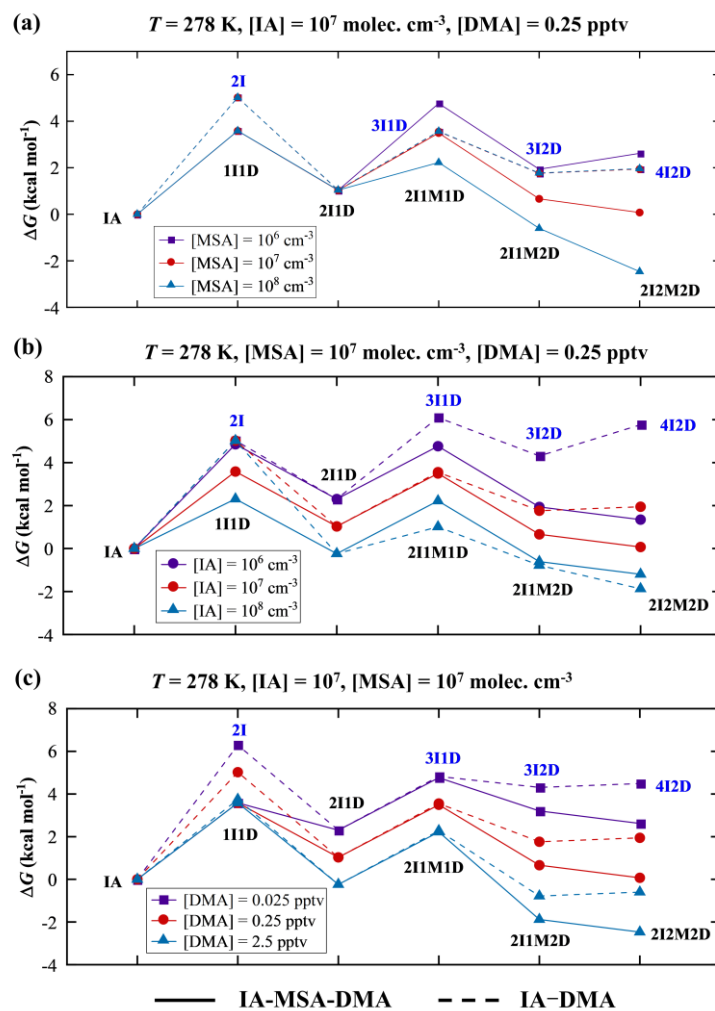


**Figure 2.** Gibbs free energies of cluster formation ( $\Delta G$ , kcal mol<sup>-1</sup>) based on the formation pathway of IA–MSA–DMA ternary (solid lines) and IA–DMA binary (dashed lines) pathways at  $T = 278$  K, (a)  $[MSA] = 10^6 - 10^8$  molec. cm<sup>-3</sup>, (b)  $[IA] = 10^6 - 10^8$  molec. cm<sup>-3</sup>, (c)  $[DMA] = 0.025 - 2.5$  pptv. I: IA, M: MSA, D: DMA.

In Fig. 2(a) ( $T = 278$  K), as  $[MSA]$  increases from  $10^6$  to  $10^8$  molec. cm<sup>-3</sup>, the barrier for the  $(IA)_2(DMA)_1 + IA \rightarrow (IA)_3(DMA)_1$  remains constant at 2.54 kcal mol<sup>-1</sup>, as this step is unaffected by MSA. In contrast,  $(IA)_2(DMA)_1 + MSA \rightarrow (IA)_2(MSA)_1(DMA)_1$  requires 3.73 kcal mol<sup>-1</sup> at  $[MSA] = 10^6$  molec. cm<sup>-3</sup>, decreases to a level comparable to  $(IA)_3(DMA)_1$  formation at  $[MSA] = 10^7$  molec. cm<sup>-3</sup> (but yields the more stable  $(IA)_2(MSA)_2(DMA)_2$  cluster), and further declines to 1.20 kcal mol<sup>-1</sup> at  $[MSA] = 10^8$  molec. cm<sup>-3</sup>. These results clearly indicate that higher  $[MSA]$  facilitates the IA–MSA–DMA ternary pathway. As shown in Fig. 2(b), at  $[IA] = 10^6$  molec. cm<sup>-3</sup>, formation of  $(IA)_2(MSA)_1(DMA)_1$  cluster (2.47 kcal mol<sup>-1</sup>) is energetically more favorable than  $(IA)_3(DMA)_1$  cluster (3.80 kcal mol<sup>-1</sup>), whereas at  $[IA] = 10^8$  molec. cm<sup>-3</sup>, the opposite occurs. This suggests that, unlike  $[MSA]$ , lower  $[IA]$  makes the IA–MSA–DMA pathway comparatively less disfavored than

the IA–DMA pathway. In Fig. 2(c), the energy barriers of the IA–MSA–DMA and IA–DMA pathways are identical at the same [DMA], as the transformation from  $(IA)_2(DMA)_1$  cluster to either  $(IA)_3(DMA)_1$  or  $(IA)_2(MSA)_1(DMA)_1$  cluster proceeds without the involvement of an additional DMA monomer. However, the resulting  $(IA)_2(MSA)_2(DMA)_2$  cluster is more stable than  $(IA)_4(DMA)_2$ , indicating that as [DMA] increases from 0.025 to 2.5 pptv, the IA–MSA–DMA pathway predominates. These results indicate that under the conditions where MSA and DMA are abundant but IA is limited, the IA–DMA pathway becomes thermodynamically unfavorable more rapidly, making the IA–MSA–DMA pathway relatively more favorable.

### 190 3.3 Cluster Formation Rate

To assess the potential synergistic enhancement, the cluster formation rate ( $J$ ,  $\text{cm}^{-3} \text{s}^{-1}$ ) of the IA–MSA–DMA system was calculated and compared with the previously reported efficient IA–DMA system (Ning et al., 2022b) using ACDC simulations. As illustrated in Fig. 3(a), the simulated  $J$  of IA–DMA and IA–MSA–DMA systems exhibit a positive correlation with increasing [IA] under the marine boundary layer (MBL) conditions of  $T = 278 \text{ K}$ ,  $CS = 2.0 \times 10^{-3} \text{ s}^{-1}$ ,  $[MSA] = 10^6 - 10^8$  molec.  $\text{cm}^{-3}$ , and  $[DMA] = 0.25 \text{ pptv}$ . In comparison, the IA–MSA–DMA system exhibits significantly higher  $J$  values than the IA–DMA system, with similar  $J$  observed only at high [IA] ( $> 10^7 \text{ molec. cm}^{-3}$ ) and low [MSA] ( $10^6 \text{ molec. cm}^{-3}$ ), showing a pronounced synergistic enhancement in nucleation. As long as [IA] drops below  $10^7 \text{ molec. cm}^{-3}$ , IA–MSA–DMA system shows markedly faster nucleation than IA–DMA system, even at the low level of [MSA] ( $10^6 \text{ molec. cm}^{-3}$ ). At a moderate [MSA] ( $10^7 \text{ molec. cm}^{-3}$ ), the  $J(\text{IA–MSA–DMA})$  reaches the order of  $10^0 - 10^2 \text{ cm}^{-3} \text{ s}^{-1}$ , which is up to  $10^3$  times higher than  $J(\text{IA–DMA})$  under the same conditions. Apart from the synergistic effects exhibited by IA–MSA–DMA ternary nucleation, we further compared the nucleation efficiencies of the binary acid–base system: IA–DMA and MSA–DMA systems. Interestingly, although IA exhibits weaker acidity compared to MSA, the resulting  $J$  of IA–DMA system significantly exceeds that of the MSA–DMA system by up to approximately four orders of magnitude at same acid levels (Fig. S3). The difference arises from the generally lower  $\Delta G$ s of IA–DMA clusters relative to MSA–DMA clusters with the same number of molecules, possibly due to the presence of not only HBs but also XBs, which provide additional structural stabilization. It should be noted that this comparison is made under equal acid concentrations to evaluate their nucleation efficiency and does not assume equal atmospheric abundances of IA and MSA. Their atmospheric concentrations are influenced by distinct sources and environmental factors, resulting in temporal and spatial heterogeneity. Taken together, these findings highlight the enhanced nucleation efficiency arising from the synergistic interactions among MSA, IA, and DMA.

210 To clarify atmospheric relevance of IA–MSA–DMA nucleation in the MBL, the simulated  $J(\text{IA–MSA–DMA})$  was compared with that of the well-established IA–iodous acid ( $\text{HIO}_2$ ) system, which has been proposed as a key nucleation mechanism in the MBL (He et al., 2021; Liu et al., 2023; Zhang et al., 2022). As shown in Fig. 3(b), at  $[MSA] = 10^7 \text{ molec. cm}^{-3}$ , the IA–MSA–DMA system exhibits notably higher  $J$  values than the IA– $\text{HIO}_2$  system at lower [IA] ( $< 4 \times 10^6 \text{ molec. cm}^{-3}$ ), although the latter slightly surpasses the former under higher [IA] conditions. However, when [MSA] increases to  $10^8 \text{ molec. cm}^{-3}$ , the values of  $J(\text{IA–MSA–DMA})$  are almost higher than the  $J(\text{IA–HIO}_2)$  at the range of [IA] ( $10^6 - 10^7 \text{ molec. cm}^{-3}$ ), with rate enhancements reaching up to four orders of magnitude. This indicates that the proposed IA–MSA–DMA

system also represents a highly efficient nucleation mechanism in the MBL. Furthermore, we compared the nucleation rates of the IA–MSA–DMA system with those of the IA–MSA–HIO<sub>2</sub> system. The results indicate that the inclusion of DMA as a strong base in the ternary system markedly enhances cluster formation. Specifically, across the studied temperature and concentration ranges, the calculated nucleation rate for the IA–MSA–DMA mechanism exceeds that of the IA–MSA–HIO<sub>2</sub> system by up to two orders of magnitude (Fig. S4). Collectively, these results highlight the critical role of the synergistic nucleation involving MSA, IA, and DMA, suggesting that IA–MSA–DMA nucleation could represent a key mechanism in the MBL. This mechanism represents a potentially important and previously overlooked NPF nucleation pathway in the MBL.

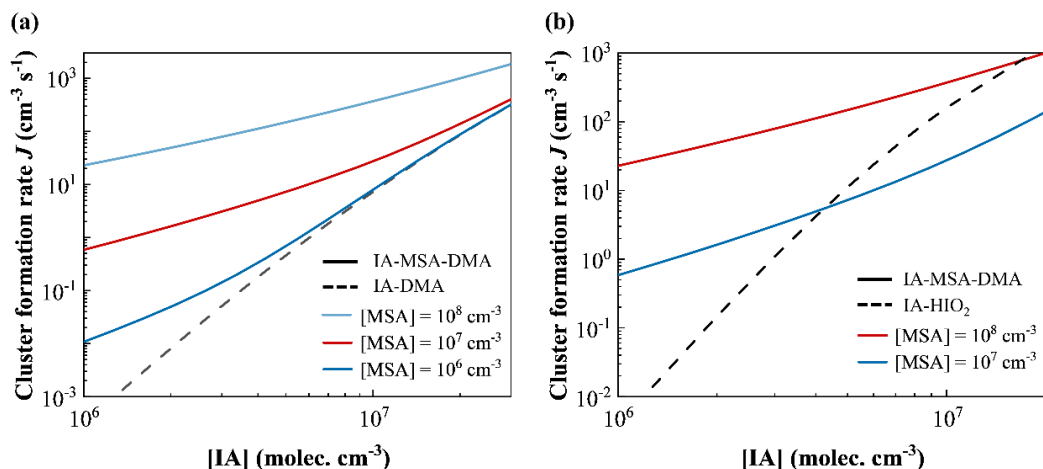


**Figure 3.** (a) Cluster formation rates  $J$  ( $\text{cm}^{-3} \text{s}^{-1}$ ) of the IA–DMA and IA–MSA–DMA systems under conditions of  $T = 278 \text{ K}$ ,  $\text{CS} = 2.0 \times 10^{-3} \text{ s}^{-1}$ ,  $[\text{IA}] = 10^6 - 3.0 \times 10^7 \text{ molec. cm}^{-3}$ ,  $[\text{MSA}] = 10^6 - 10^8 \text{ molec. cm}^{-3}$ , and  $[\text{DMA}] = 0.25 \text{ pptv}$ ; (b)  $J$  of the IA–HIO<sub>2</sub> and IA–MSA–DMA systems under conditions of  $T = 278 \text{ K}$ ,  $\text{CS} = 2.0 \times 10^{-3} \text{ s}^{-1}$ ,  $[\text{IA}] = 10^6 - 2.0 \times 10^7 \text{ molec. cm}^{-3}$ ,  $[\text{MSA}] = 10^7 - 10^8 \text{ molec. cm}^{-3}$ , and  $[\text{DMA}] = 0.25 \text{ pptv}$ .  $[\text{IA}]/[\text{HIO}_2]$  is fixed at a value of 50.

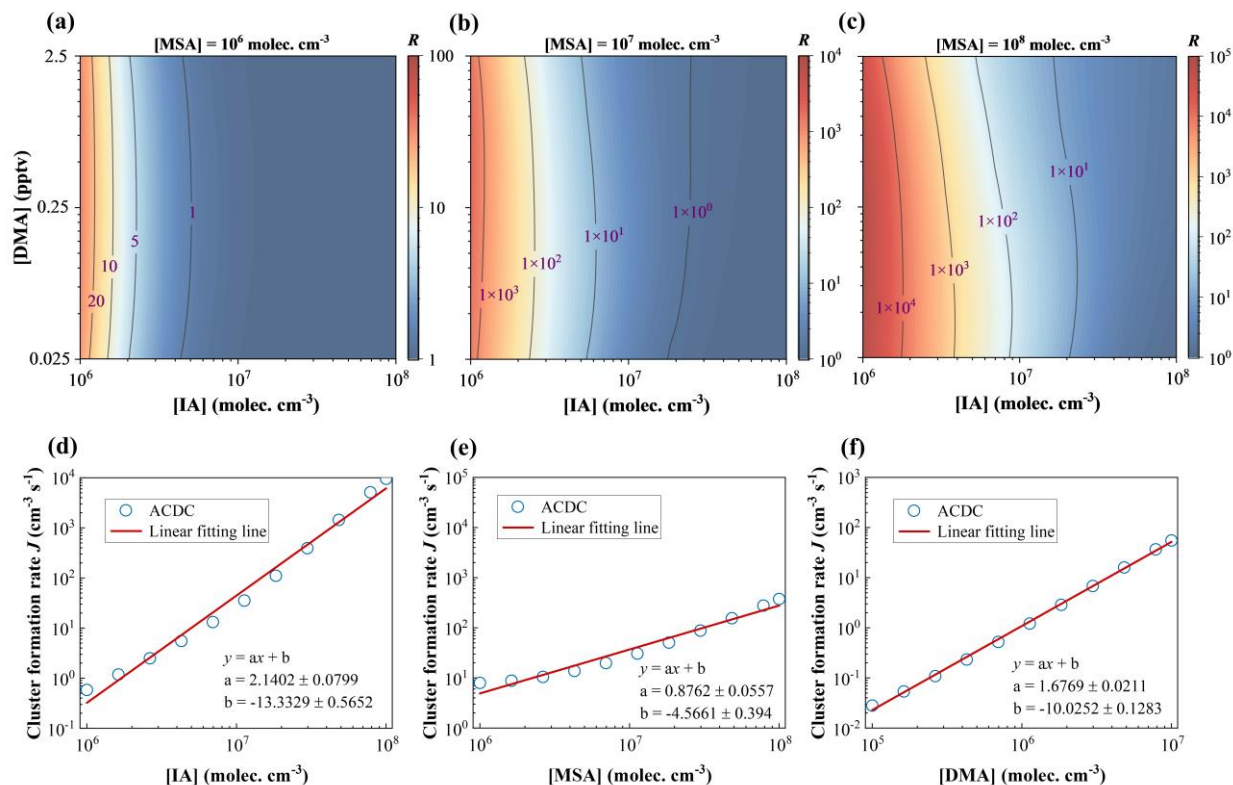
Additionally, to account for potential uncertainties in quantum chemical calculations and cluster dynamic simulations, we also examined the effects of the calculated  $\Delta G$  of clusters and the enhancement factor (sticking factor, SF) on  $J$ . As shown in Fig. S5, under boundary-layer conditions, variations in the  $\Delta G$  ( $\pm 0.2 \text{ kcal mol}^{-1}$ ) (Liakos et al., 2020) of clusters and the SF (2.1 – 2.5) in dynamic simulations lead to only minor changes in  $J$ .

### 3.4 Synergistic Nucleation of IA, MSA, and DMA

As discussed above, the IA–MSA–DMA system shows a synergistic effect on nucleation, resulting in an enhancement on  $J$ . To assess this, the included binary acid-base systems, i.e., IA–DMA and MSA–DMA nucleation, were selected as a reference for comparison. Herein, we accordingly define the enhancement factor  $R$  as the ratio of  $J(\text{IA–MSA–DMA})$  to  $[J(\text{IA–DMA}) + J(\text{MSA–DMA})]$  (Eq. (4)).

$$R = \frac{J(\text{IA–MSA–DMA})}{J(\text{IA–DMA}) + J(\text{MSA–DMA})} = \frac{J([\text{IA}] = x, [\text{MSA}] = y, [\text{DMA}] = z)}{J([\text{IA}] = x, [\text{MSA}] = 0, [\text{DMA}] = z) + J([\text{IA}] = 0, [\text{MSA}] = y, [\text{DMA}] = z)}, \quad (4)$$

where  $x$ ,  $y$ , and  $z$  denote the concentrations of IA, MSA, and DMA, respectively.



240

**Figure 4.** Enhancement factor  $R$  for IA–MSA–DMA cluster formation under conditions of  $T = 278$  K,  $CS = 2.0 \times 10^{-3} \text{ s}^{-1}$ ,  $[IA] = 10^6 - 10^8$  molec.  $\text{cm}^{-3}$ ,  $[DMA] = 0.025 - 2.5$  pptv, and (a)  $[MSA] = 10^6$ , (b)  $10^7$ , and (c)  $10^8$  molec.  $\text{cm}^{-3}$ , respectively. Function dependence of the cluster formation rate ( $J$ ) on (d)  $[IA]$  ( $r = 0.99$ ), (e)  $[MSA]$  ( $r = 0.98$ ), and (f)  $[DMA]$  ( $r = 0.99$ ), showing a linear relationship.

245

As shown in Fig. 4(a-c), the calculated  $R$  increases with rising MSA levels ( $10^6$  to  $10^8$  molec.  $\text{cm}^{-3}$ ), spanning 1 to 4 orders of magnitude, highlight the efficiency of ternary nucleation. In contrast, with  $[MSA]$  and  $[DMA]$  held constant,  $R$  decreases markedly as  $[IA]$  increases. This trend aligns with Fig. 3(a), where the gap between  $J(\text{IA-MSA-DMA})$  and  $J(\text{IA-DMA})$  narrows with rising  $[IA]$ . It may be explained by IA's higher efficiency in binding DMA compared to MSA (recalling Sect. 3.3 and Fig. S3), coupled with higher  $[IA]$ , which amplifies the role of IA–DMA nucleation. It is noteworthy that the contribution of  $J(\text{MSA-DMA})$  is negligible, as it is 4–7 orders of magnitude lower than  $J(\text{IA-DMA})$ . While  $R$  is less sensitive to  $[DMA]$  compared to  $[IA]$ , likely due to the relatively narrow range of  $[DMA]$  in atmosphere, which constrains its impact. Overall, the  $R$  gradually decreases with increasing  $[IA]$ . However, at higher  $[MSA]$ , a slight increase in  $R$  is observed, as the presence of MSA counteracts the dominance of the strong IA–DMA binding and enhances the stability of the ternary clusters.

250

255

These findings suggest that IA–MSA–DMA synergistic nucleation is most relevant in iodine-limited, sulfur-, and nitrogen-rich regions. In addition, the IA–MSA–DMA synergistic nucleation rate shows a sensitivity ranking of  $IA > DMA > MSA$  with respect to their concentration variations (Fig. 4(d-f)). The three-dimensional response surface also shows that when the

concentration of any one precursor is held constant, the  $J$  increases with the concentration of the other two precursors, indicating significant sensitivity to variations in each component. However,  $J$  responds most rapidly to changes in [IA], followed by [DMA], while the response to [MSA] is the slowest (Fig. S6).

### 3.5 Cluster Formation Pathway

260 As indicated by the rate analyses, the IA–MSA–DMA synergy enhances nucleation; however, the underlying clustering pathways and their corresponding contribution to particle formation remain unresolved, necessitating further analysis to clarify nucleation dynamics.

As illustrated in Fig. 5(a), under the potential MBL conditions of  $T = 278$  K,  $CS = 2.0 \times 10^{-3} \text{ s}^{-1}$ ,  $[IA] = 10^7 \text{ molec. cm}^{-3}$ ,  $[MSA] = 10^7 \text{ molec. cm}^{-3}$ , and  $[DMA] = 0.25 \text{ pptv}$ , the cluster formation pathways of IA–MSA–DMA system can be classified  
265 into two types: IA–DMA binary pathway and IA–MSA–DMA ternary pathway. Specifically, IA–DMA clustering pathway proceeds primarily by sequential collisions of IA and DMA monomers, ultimately forming  $(IA)_4(DMA)_2$  cluster that is recognized as the boundary cluster (see details in the SI), which can grow beyond the simulation system. The dominant nucleation mechanism identified in the ternary IA–MSA–DMA system involves two types of pathways: the ternary IA–MSA–DMA pathway and the binary IA–DMA pathway, the latter of which is similar to the pattern reported by Ning et al. (2022b).

270 In contrast, the ternary IA–MSA–DMA clustering pathway is more complex. In addition to a stepwise growth route similar to the binary IA–DMA pathway via  $(IA)_2(DMA)_1$  cluster, IA monomer can also collide with MSA monomer to form a  $(IA)_1(MSA)_1$  heterodimer. The formed  $(IA)_1(MSA)_1$  cluster can further collide with DMA monomer to form a  $(IA)_1(MSA)_1(DMA)_1$  heterotrimer, which can grow via two routes: a) colliding with an IA monomer to produce a  $(IA)_2(MSA)_1(DMA)_1$  cluster; b) colliding with a MSA monomer to form a  $(IA)_1(MSA)_2(DMA)_1$  cluster. The two clusters can  
275 continue to grow, ultimately yielding a  $(IA)_2(MSA)_2(DMA)_2$  cluster, which can grow larger to contribute to particle formation. At elevated temperatures of 288 – 298 K, the IA–MSA–DMA ternary nucleation pathway exhibits notable modifications. As illustrated in Fig. S7, both IA and MSA monomers are capable of alternately colliding with other monomers, ultimately yielding the  $(IA)_1(MSA)_2(DMA)_3$  cluster that subsequently undergoes further growth.

To further quantify the relative contributions of different clustering pathways, we performed ACDC simulations to track  
280 the molecular-level clustering processes under varying precursor concentrations and temperatures. As shown in Fig. 5(b), the contribution of the IA–MSA–DMA pathway (yellow bar) exhibits a pronounced positive dependence on both [MSA] and [DMA]. Specifically, as [MSA] increases from  $5.0 \times 10^5$  to  $5.0 \times 10^7 \text{ molec. cm}^{-3}$ , the contribution of IA–MSA–DMA pathway rises sharply from 3% to 98%. Similarly, increasing [DMA] from  $2.5 \times 10^{-3}$  to  $2.5 \times 10^{-2} \text{ pptv}$  results in a substantial enhancement of the pathway contribution from 20% to 67%; however, further elevation of [DMA] to  $2.5 \times 10^{-1}$  and  $2.5 \times 10^0$   
285 pptv induces only marginal changes, suggesting a base saturation effect. In contrast, the contribution of the IA–MSA–DMA pathway is negatively correlated with [IA]. At [IA] below  $10^7 \text{ molec. cm}^{-3}$ , the ternary IA–MSA–DMA pathway predominates, whereas at [IA] above this threshold, the binary IA–DMA pathway becomes dominant. Temperature also exerts a significant influence: as the temperature increases from 258 K to 298 K, the relative contribution of the IA–MSA–DMA pathway

decreases markedly, with an abrupt decline observed between 278 K and 288 K. This may be attributed to a distinct change in the growth pattern of the IA–MSA–DMA pathway when the temperature rises to 288 – 298 K (Fig. S7). Specifically, the dominant growing cluster shifts from  $(IA)_2(MSA)_2(DMA)_2$  at 278 K to  $(IA)_1(MSA)_2(DMA)_3$  at 288–298 K, indicating temperature would influence the cluster growth pathway.

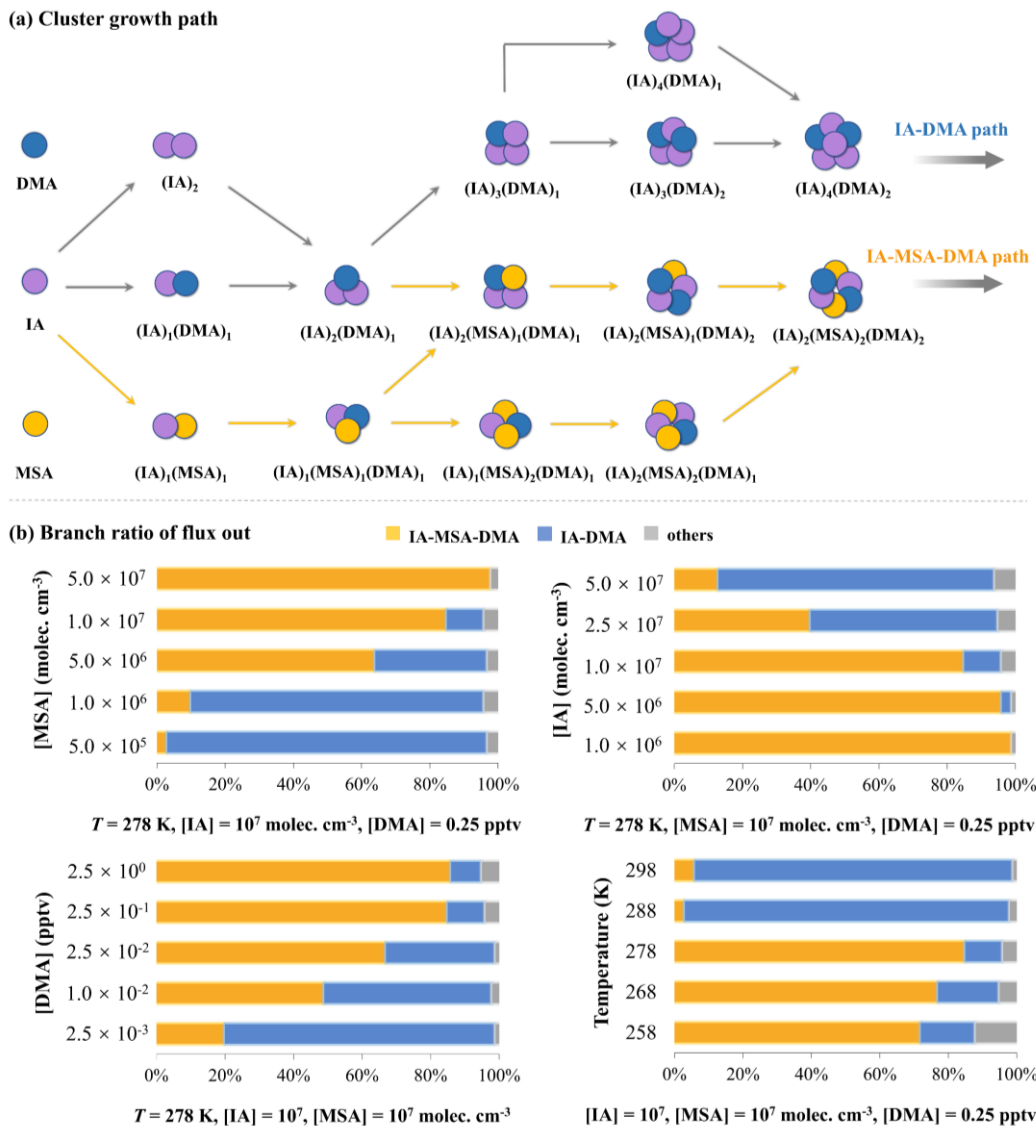


**Figure 5. (a)** The simulated primary cluster growth pathways of IA–MSA–DMA system at the conditions of  $T = 278$  K,  $CS = 2.0 \times 10^{-3} s^{-1}$ ,  $[IA] = 10^7$  molec.  $cm^{-3}$ ,  $[MSA] = 10^7$  molec.  $cm^{-3}$ , and  $[DMA] = 0.25$  pptv; **(b)** Branch ratio of different flux out under the varying  $[MSA]$  ( $5.0 \times 10^5 - 5.0 \times 10^7$  molec.  $cm^{-3}$ ),  $[IA]$  ( $1.0 \times 10^6 - 5.0 \times 10^7$  molec.  $cm^{-3}$ ),  $[DMA]$  ( $2.5 \times 10^{-3} - 2.5 \times 10^0$  pptv), and temperatures (258 – 298 K).

Overall, these results demonstrate that the IA–MSA–DMA pathway is highly sensitive to precursor concentrations and temperatures. Its contribution increases strongly with [MSA] and moderately with [DMA] until a saturation effect is reached, while exhibiting a negative dependence on [IA]. Temperature rise significantly suppresses the role of this ternary pathway, especially around 278 – 288 K. Therefore, this synergistic nucleation involving sulfur (MSA), iodine (IA), and nitrogen (DMA) precursors is most prevalent in cold environments that are rich in sulfur and nitrogen but scarce in iodine, such as polar marine regions. This is consistent with previous studies indicating that the MSA formation is highly temperature-dependent and is enhanced in polar areas (Chen et al., 2023; Scholz et al., 2023), while IA concentrations tend to decrease at high latitudes with lower temperatures, as reflected in the observed decline of iodine monoxide (a key IA precursor) with increasing latitude (Takashima et al., 2022).

### 3.6 Comparison with Field Observations

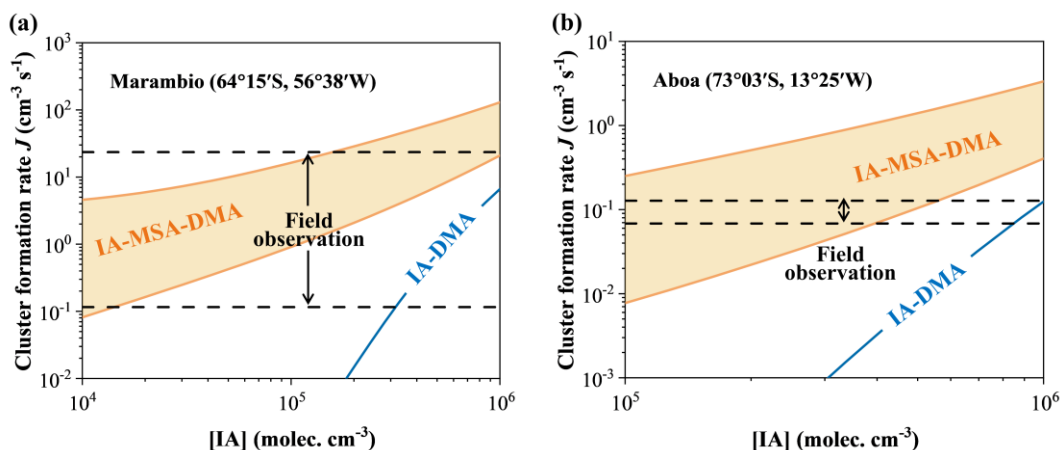
To better evaluate the potential atmospheric implications of the proposed IA–MSA–DMA nucleation mechanism, we calculated the cluster formation rate under polar conditions, where the impact of IA–MSA–DMA nucleation is expected to be significant, and further compared the simulations with field observations. As discussed earlier, the IA–MSA–DMA synergistic nucleation is relatively impactful in the cold coastal regions, where [MSA] is relatively higher and [IA] is lower. Accordingly, Marambio and Aboa were selected for a comparative analysis due to their shared characteristics: both sites are located in coastal polar regions, exhibit high [MSA] levels but relatively low [IA], and have low annual mean temperatures ( $\leq 273$  K) (Quéléver et al., 2022; Xavier et al., 2024).

As illustrated in Fig. 6(a), the  $J(\text{IA–MSA–DMA})$  was simulated under the representative atmospheric conditions of  $T = 273$  K,  $\text{CS} = 10^{-4} \text{ s}^{-1}$ ,  $[\text{IA}] = 10^4 - 10^6 \text{ molec. cm}^{-3}$ ,  $[\text{MSA}] = 10^6 - 10^7 \text{ molec. cm}^{-3}$ , and  $[\text{DMA}] = 2.0 \text{ pptv}$  (Quéléver et al., 2022; He et al., 2021; Yu and Luo, 2014). The simulated values of  $J$  were then compared with field-measured nucleation rates at the coastal Antarctic station Marambio. The results show that, for both the IA–DMA and IA–MSA–DMA systems, the  $J$  increases monotonically with [IA]. Notably, the incorporation of MSA markedly enhances the formation rates (orange-shaded region), bringing them into closer alignment with the observed nucleation rate range ( $0.12 - 24 \text{ cm}^{-3} \text{ s}^{-1}$ , black dashed lines) (Quéléver et al., 2022). Even at the lower bound of [MSA] ( $10^6 \text{ molec. cm}^{-3}$ , lower orange solid line), the simulated formation rates still match or exceed the minimum observed value ( $0.12 \text{ cm}^{-3} \text{ s}^{-1}$ , lower black dashed line). Moreover, at lower IA levels, the effect of MSA is pronounced, and ternary nucleation driven by synergistic effects can effectively capture the observed nucleation rates. Conversely, under high [IA], the contribution of the IA–DMA pathway becomes increasingly prominent and can account for a portion of the nucleation rate. Overall, the MSA-enhanced ternary nucleation appears capable of reproducing the nucleation rates observed at Marambio across the measured range of [IA], particularly under high-rate conditions. Even at the highest IA levels, this reproduction cannot be fully captured by the IA–DMA binary mechanism alone.

A further comparison was conducted under conditions representative of the Aboa station, at  $T = 268$  K,  $\text{CS} = 10^{-4} \text{ s}^{-1}$ ,  $[\text{IA}] = 10^5 - 10^6 \text{ molec. cm}^{-3}$ ,  $[\text{MSA}] = 10^6 - 10^7 \text{ molec. cm}^{-3}$ , and  $[\text{DMA}] = 0.055 \text{ pptv}$  (Xavier et al., 2024; He et al., 2021; Yu and Luo, 2014), with the corresponding results shown in Fig. 6(b). The simulated  $J$  values of the IA–MSA–DMA system

partially overlap with the field observation rates ( $0.07 - 0.13 \text{ cm}^{-3} \text{ s}^{-1}$ , black dashed lines) (Xavier et al., 2024), whereas the simulated  $J(\text{IA-DMA})$  values deviate considerably from the observations. These results underscore the potential importance of the synergistic nucleation of sulfur-, iodine-, and nitrogen-containing compounds in cold polar marine environments, particularly during periods of elevated sulfur compound concentrations associated with NPF events.

335 It should be noted that the nucleation rates presented here, particularly at the upper end of the studied concentration ranges, represent the theoretical results under ideal conditions of concurrently high precursor levels. In the marine atmosphere, temporal and spatial variations in the concentrations of IA, MSA, and DMA will modulate the rates. Nevertheless, our proposed synergistic mechanism of the ternary IA-MSA-DMA nucleation provides a critical mechanistic understanding for periods and regions where these precursors co-exist at significant levels.



340 **Figure 6.** Comparison with the simulated cluster formation rate ( $J$ ,  $\text{cm}^{-3} \text{ s}^{-1}$ ) and field observations under the ambient conditions: (a) Marambio ( $T = 273 \text{ K}$ ,  $\text{CS} = 10^{-4} \text{ s}^{-1}$ ,  $[\text{IA}] = 10^4 - 10^6 \text{ molec. cm}^{-3}$ ,  $[\text{MSA}] = 10^6 - 10^7 \text{ molec. cm}^{-3}$ , and  $[\text{DMA}] = 2.0 \text{ pptv}$ ) and (b) Aboa ( $T = 268 \text{ K}$ ,  $\text{CS} = 10^{-4} \text{ s}^{-1}$ ,  $[\text{IA}] = 10^5 - 10^6 \text{ molec. cm}^{-3}$ ,  $[\text{MSA}] = 10^6 - 10^7 \text{ molec. cm}^{-3}$ , and  $[\text{DMA}] = 0.055 \text{ pptv}$ ). The orange area, blue line, and black line represent  $J(\text{IA-MSA-DMA})$ ,  $J(\text{IA-DMA})$ , and  $J(\text{field observation})$ , respectively. The shaded area corresponds to the nucleation rates simulated at  $[\text{MSA}] = 10^6 - 10^7 \text{ molec. cm}^{-3}$ . The dashed field-observation ranges for  $J$  at Marambio ( $0.1 - 24 \text{ cm}^{-3} \text{ s}^{-1}$ ) and Aboa ( $0.07 - 0.13 \text{ cm}^{-3} \text{ s}^{-1}$ ) are based on the reported  $J_{1.5}$  values from Qu  l  ver et al. (2022) and Jokinen et al. (2018), respectively.

#### 4 Conclusion

Marine aerosol significantly influences the Earth's radiative balance and climate system, yet the fundamental nucleation mechanism in aerosol formation is highly unclear. Despite the recognition of sulfur-, iodine-, and nitrogen-containing chemicals as vital nucleating precursors, whether they can interact and synergistically contribute to nucleation remains unknown.

To address this gap, we systematically investigated the ternary nucleation system involving methanesulfonic acid (MSA, sulfur-containing), iodic acid (IA, iodine-containing), and dimethylamine (DMA, nitrogen-containing) via high-level quantum

chemical calculations and atmospheric cluster dynamics simulations. The main findings of this study are as follows: (1) the  
355 stable prenucleation cluster composed of IA, MSA, and DMA is mainly stabilized by intermolecular hydrogen bonds (74%),  
together with contributions from halogen bonding (XB) and electrostatic attractions between ion pairs produced via acid-base  
reactions (i.e.,  $\text{CH}_3\text{SO}_3^-$ -DMAH<sup>+</sup> and  $\text{IO}_3^-$ -DMAH<sup>+</sup>). (2) The nucleation dynamics of the IA-MSA-DMA system exhibits a  
pronounced synergistic effect, leading to an enhancement in nucleation rates by 4–8 orders of magnitude compared with the  
included binary IA-DMA or MSA-DMA systems; under sulfur-rich conditions, the resulting rate even surpasses that of the  
360 efficient IA-iodous acid (HIO<sub>2</sub>) nucleation mechanism. (3) Mechanistic analysis indicates that the IA-MSA-DMA ternary  
nucleation is most evident under cold, sulfur- and nitrogen-rich conditions, and the simulated rates under polar-site conditions  
(Marambio and Aboa) align well with field observations, advancing our understanding of NPF events.

These results advance our understanding of marine nucleation by highlighting the synergistic role of sulfur, iodine, and  
nitrogen precursors—an effect that was previously ignored in binary nucleation frameworks. Incorporating the IA-MSA-  
365 DMA mechanism into atmospheric models can refine parameterizations of marine aerosol formation, reducing uncertainties  
in climate forcing predictions.

**Data availability.** The data in this article are available from the corresponding author upon reasonable request  
(anning@bit.edu.cn and zhangxiuhui@bit.edu.cn).

**Supplement.** The supplement related to this article is available online at :

370 **Author contribution.** XZ designed and supervised the research. JL, XD, and AN performed the quantum chemical  
calculations and the ACDC simulations. JL, AN, and LL analyzed data. JL, AN, and XZ wrote the paper with contributions  
from all the other co-authors.

**Competing interests.** The contact author has declared that neither they nor their co-authors have any competing interests.

375 **Disclaimer.** Publisher's note: Copernicus Publications remains neutral with regard to jurisdictional claims in published maps  
and institutional affiliations.

**Acknowledgement.** This work is funded by the National Science Fund for Distinguished Young Scholars (grant no. 22225607),  
the National Natural Science Foundation of China (grant nos. 22306011 and 22376013), and the China Postdoctoral Science

Foundation (grant no. 2025M784255). Furthermore, we thank for the technical support of the National Large Scientific and Technological Infrastructure “Earth System Numerical Simulation Facility” (<https://cstr.cn/31134.02.EL>).

380 **Financial support.** This work is supported by the National Science Fund for Distinguished Young Scholars (grant no. 22225607), the National Natural Science Foundation of China (grant nos. 22306011 and 22376013), and the China Postdoctoral Science Foundation (grant no. 2025M784255).

## References

- Almeida, J., Schobesberger, S., Kürten, A., Ortega, I. K., Kupiainen-Määttä, O., Praplan, A. P., Adamov, A., Amorim, A.,  
385 Bianchi, F., Breitenlechner, M., David, A., Dommen, J., Donahue, N. M., Downard, A., Dunne, E., Duplissy, J., Ehrhart, S., Flagan, R. C., Franchin, A., Guida, R., Hakala, J., Hansel, A., Heinritzi, M., Henschel, H., Jokinen, T., Junninen, H., Kajos, M., Kangasluoma, J., Keskinen, H., Kupc, A., Kurten, T., Kvashin, A. N., Laaksonen, A., Lehtipalo, K., Leiminger, M., Leppä, J., Loukonen, V., Makhmutov, V., Mathot, S., McGrath, M. J., Nieminen, T., Olenius, T., Onnela, A., Petäjä, T., Riccobono, F., Riipinen, I., Rissanen, M., Rondo, L., Ruuskanen, T., Santos, F. D., Sarnela, N., Schallhart, S.,  
390 Schnitzhofer, R., Seinfeld, J. H., Simon, M., Sipilä, M., Stozhkov, Y., Stratmann, F., Tomé, A., Tröstl, J., Tsagkogeorgas, G., Vaattovaara, P., Viisanen, Y., Virtanen, A., Vrtala, A., Wagner, P. E., Weingartner, E., Wex, H., Williamson, C., Wimmer, D., Ye, P., Yli-Juuti, T., Carslaw, K. S., Kulmala, M., Curtius, J., Baltensperger, U., Worsnop, D. R., Vehkamäki, H. and Kirkby, J.: Molecular understanding of sulphuric acid-amine particle nucleation in the atmosphere, *Nature*, 502, 359–363, <http://doi.org/10.1038/nature12663>, 2013.
- 395 Baccarini, A., Karlsson, L., Dommen, J., Duplessis, P., Vullers, J., Brooks, I. M., Saiz-Lopez, A., Salter, M., Tjernstrom, M., Baltensperger, U., Zieger, P. and Schmale, J.: Frequent new particle formation over the high Arctic pack ice by enhanced iodine emissions, *Nat. Commun.*, 11, 4924, <http://doi.org/10.1038/s41467-020-18551-0>, 2020.
- Beck, L. J., Sarnela, N., Junninen, H., Hoppe, C. J. M., Garmash, O., Bianchi, F., Riva, M., Rose, C., Peräkylä, O., Wimmer, D., Kausiala, O., Jokinen, T., Ahonen, L., Mikkilä, J., Hakala, J., He, X. C., Kontkanen, J., Wolf, K. K. E., Cappelletti, D.,  
400 Mazzola, M., Traversi, R., Petroselli, C., Viola, A. P., Vitale, V., Lange, R., Massling, A., Nøjgaard, J. K., Krejci, R., Karlsson, L., Zieger, P., Jang, S., Lee, K., Vakkari, V., Lampilahti, J., Thakur, R. C., Leino, K., Kangasluoma, J., Duplissy, E. M., Siivola, E., Marbouti, M., Tham, Y. J., Saiz-Lopez, A., Petäjä, T., Ehn, M., Worsnop, D. R., Skov, H., Kulmala, M., Kerminen, V. M. and Sipilä, M.: Differing Mechanisms of New Particle Formation at Two Arctic Sites, *Geophys. Res. Lett.*, 48, e2020GL091334, <http://doi.org/10.1029/2020gl091334>, 2021.
- 405 Berresheim, H., Elste, T., Rosman, K., Dal Maso, M., Tremmel, H. G., Mäkelä, J. M., Allen, A. G., Kulmala, M. and Hansson, H.-C.: Gas-aerosol relationships of H<sub>2</sub>SO<sub>4</sub>, MSA, and OH: Observations in the coastal marine boundary layer at Mace Head, Ireland, *J. Geophys. Res.-Atmos.*, 107, PAR 5-1–PAR 5-12, <http://doi.org/10.1029/2000jd000229>, 2002.

- Cai, R., Yan, C., Yang, D., Yin, R., Lu, Y., Deng, C., Fu, Y., Ruan, J., Li, X., Kontkanen, J., Zhang, Q., Kangasluoma, J., Ma, Y., Hao, J., Worsnop, D. R., Bianchi, F., Paasonen, P., Kerminen, V.-M., Liu, Y., Wang, L., Zheng, J., Kulmala, M. and Jiang, J.: Sulfuric acid–amine nucleation in urban Beijing, *Atmos. Chem. Phys.*, 21, 2457–2468, <http://doi.org/10.5194/acp-21-2457-2021>, 2021.
- Chan, B. and Yim, W. L.: Accurate Computation of Cohesive Energies for Small to Medium-Sized Gold Clusters, *J. Chem. Theory Comput.*, 9, 1964–1970, <http://doi.org/10.1021/ct400047y>, 2013.
- Chen, H. and Finlayson-Pitts, B. J.: New Particle Formation from Methanesulfonic Acid and Amines/Ammonia as a Function of Temperature, *Environ Sci Technol*, 51, 243–252, <http://doi.org/10.1021/acs.est.6b04173>, 2017.
- Chen, H., Varner, M. E., Gerber, R. B. and Finlayson-Pitts, B. J.: Reactions of Methanesulfonic Acid with Amines and Ammonia as a Source of New Particles in Air, *J. Phys. Chem. B*, 120, 1526–1536, <http://doi.org/10.1021/acs.jpcc.5b07433>, 2016.
- Chen, J., Lane, J. R., Bates, K. H. and Kjaergaard, H. G.: Atmospheric Gas-Phase Formation of Methanesulfonic Acid, *Environ. Sci. Technol.*, 57, 21168–21177, <http://doi.org/10.1021/acs.est.3c07120>, 2023.
- Chen, Q., Sherwen, T., Evans, M. and Alexander, B.: DMS oxidation and sulfur aerosol formation in the marine troposphere: a focus on reactive halogen and multiphase chemistry, *Atmos. Chem. Phys.*, 18, 13617–13637, <http://doi.org/10.5194/acp-18-13617-2018>, 2018.
- Dal Maso, M., Kulmala, M., Lehtinen, K. E. J., Mäkelä, J. M., Aalto, P. and O’Dowd, C. D.: Condensation and coagulation sinks and formation of nucleation mode particles in coastal and boreal forest boundary layers, *J. Geophys. Res.-Atmos.*, 107, PAR 2-1–PAR 2-10, <http://doi.org/10.1029/2001jd001053>, 2002.
- Dawson, M. L., Varner, M. E., Perraud, V., Ezell, M. J., Gerber, R. B. and Finlayson-Pitts, B. J.: Simplified mechanism for new particle formation from methanesulfonic acid, amines, and water via experiments and ab initio calculations, *Proc. Natl. Acad. Sci. U. S. A.*, 109, 18719–18724, <http://doi.org/10.1073/pnas.1211878109>, 2012.
- Eisele, F. L. and Tanner, D. J.: Measurement of the gas phase concentration of H<sub>2</sub>SO<sub>4</sub> and methane sulfonic acid and estimates of H<sub>2</sub>SO<sub>4</sub> production and loss in the atmosphere, *J. Geophys. Res.*, 98, 9001–9010, <http://doi.org/10.1029/93JD00031>, 1993.
- Elm, J.: Clusteromics II: Methanesulfonic acid–base cluster formation, *ACS Omega*, 6, 17035–17044, <http://doi.org/10.1021/acsomega.1c02115>, 2021.
- Engsvang, M. and Elm, J.: Iodine Clusters in the Atmosphere II: Cluster Formation Potential of Iodine Oxyacids and Iodine Oxides, *ACS Omega*, 10, 24887–24896, <http://doi.org/10.1021/acsomega.5c02147>, 2025.
- Engsvang, M., Wu, H. and Elm, J.: Iodine clusters in the atmosphere I: Computational benchmark and dimer formation of oxyacids and oxides, *ACS Omega*, 9, 31521–31532, <http://doi.org/10.1021/acsomega.4c01235>, 2024.
- Francl, M. M., Pietro, W. J., Hehre, W. J., Binkley, J. S., Gordon, M. S., DeFrees, D. J. and Pople, J. A.: Self-consistent molecular orbital methods. XXIII. A polarization-type basis set for second-row elements, *J. Chem. Phys.*, 77, 3654–3665, <http://doi.org/10.1063/1.444267>, 1982.

- Frisch, M. J., Trucks, G. W., Schlegel, H. B., Scuseria, G. E., Robb, M. A., Cheeseman, J. R., Scalmani, G., Barone, V., Mennucci, B., Petersson, G. A., Nakatsuji, H., Caricato, M., Li, X., Hratchian, H. P., Izmaylov, A. F., Bloino, J., Zheng, G., Sonnenberg, J. L., Hada, M., Ehara, M., Toyota, K., Fukuda, R., Hasegawa, J., Ishida, M., Nakajima, T., Honda, Y., Kitao, O., Nakai, H., Vreven, T., Montgomery, J. A., Peralta, J. E., Ogliaro, F., Bearpark, M., Heyd, J. J., Brothers, E., Kudin, K. N., Staroverov, V. N., Kobayashi, R., Normand, J., Raghavachari, K., Rendell, A., Burant, J. C., Iyengar, S. S., Tomasi, J., Cossi, M., Rega, N., Millam, J. M., Klene, M., Knox, J. E., Cross, J. B., Bakken, V., Adamo, C., Jaramillo, J., Gomperts, R., Stratmann, R. E., Yazyev, O., Austin, A. J., Cammi, R., Pomelli, C., Ochterski, J. W., Martin, R. L., Morokuma, K., Zakrzewski, V. G., Voth, G. A., Salvador, P., Dannenberg, J. J., Dapprich, S., Daniels, A. D., Farkas, O., Foresman, J. B., Ortiz, J. V., Cioslowski, J. and Fox, D. J.: Gaussian 09, Revision A.02, Gaussian Inc, Wallingford CT, <http://gaussian.com/g09citation/> (last access: 07 May 2022), 2009.
- 445
- Frisch, M. J., Trucks, G. W., Schlegel, H. B., Scuseria, G. E., Robb, M. A., Cheeseman, J. R., Scalmani, G., Barone, V., Mennucci, B., Petersson, G. A., Nakatsuji, H., Caricato, M., Li, X., Hratchian, H. P., Izmaylov, A. F., Bloino, J., Zheng, G., Sonnenberg, J. L., Hada, M., Ehara, M., Toyota, K., Fukuda, R., Hasegawa, J., Ishida, M., Nakajima, T., Honda, Y., Kitao, O., Nakai, H., Vreven, T., Montgomery, J. A., Peralta, J. E., Ogliaro, F., Bearpark, M., Heyd, J. J., Brothers, E., Kudin, K. N., Staroverov, V. N., Kobayashi, R., Normand, J., Raghavachari, K., Rendell, A., Burant, J. C., Iyengar, S. S., Tomasi, J., Cossi, M., Rega, N., Millam, J. M., Klene, M., Knox, J. E., Cross, J. B., Bakken, V., Adamo, C., Jaramillo, J., Gomperts, R., Stratmann, R. E., Yazyev, O., Austin, A. J., Cammi, R., Pomelli, C., Ochterski, J. W., Martin, R. L., Morokuma, K., Zakrzewski, V. G., Voth, G. A., Salvador, P., Dannenberg, J. J., Dapprich, S., Daniels, A. D., Farkas, O., Foresman, J. B., Ortiz, J. V., Cioslowski, J. and Fox, D. J.: Gaussian 16, Revision A.03, Gaussian Inc, Wallingford CT, <https://gaussian.com/gaussian16/> (last access: 20 November 2023), 2016.
- 450
- 455
- 460
- Gottelman, A. and Kahn, R.: Aerosols are critical for “nowcasting” climate, *One Earth*, 8, 101239, <http://doi.org/10.1016/j.oneear.2025.101239>, 2025.
- Halonen, R., Zapadinsky, E., Kurtén, T., Vehkamäki, H. and Reischl, B.: Rate enhancement in collisions of sulfuric acid molecules due to long-range intermolecular forces, *Atmos. Chem. Phys.*, 19, 13355–13366, <http://doi.org/10.5194/acp-19-13355-2019>, 2019.
- 465
- He, X.-C., Simon, M., Iyer, S., Xie, H.-B., Rörup, B., Shen, J., Finkenzeller, H., Stolzenburg, D., Zhang, R., Baccarini, A., Tham, Y. J., Wang, M., Amanatidis, S., Piedehierro, A. A., Amorim, A., Baalbaki, R., Brasseur, Z., Caudillo, L., Chu, B., Dada, L., Duplissy, J., Haddad, I. E., Flagan, R. C., Granzin, M., Hansel, A., Heinritzi, M., Hofbauer, V., Jokinen, T., Kempainen, D., Kong, W., Krechmer, J., Kürten, A., Lamkaddam, H., Lopez, B., Ma, F., Mahfouz, N. G. A., Makhmutov, V., Manninen, H. E., Marie, G., Marten, R., Massabò, D., Mauldin, R. L., Mentler, B., Onnela, A., Petäjä, T., Pfeifer, J., Philippov, M., Ranjithkumar, A., Rissanen, M. P., Schobesberger, S., Scholz, W., Schulze, B., Surdu, M., Thakur, R. C., Tomé, A., Wagner, A. C., Wang, D., Wang, Y., Weber, S. K., Welti, A., Winkler, P. M., Zauner-Wieczorek, M., Baltensperger, U., Curtius, J., Kurtén, T., Worsnop, D. R., Volkamer, R., Lehtipalo, K., Kirkby, J., Donahue, N. M., Sipilä,
- 470

- M. and Kulmala, M.: Iodine oxoacids enhance nucleation of sulfuric acid particles in the atmosphere, *Science*, 382, 1308–1314, <http://doi.org/10.1126/science.adh2526>, 2023.
- 475 He, X.-C., Tham, Y. J., Dada, L., Wang, M., Finkenzeller, H., Stolzenburg, D., Iyer, S., Simon, M.,  rten, A. K., Shen, J., Roerup, B., Rissanen, M., Schobesberger, S., Baalbaki, R., Wang, D. S., Koenig, T. K., Jokinen, T., Sarnela, N., Beck, L. J., Almeida, J., Amanatidis, S., Amorim, A., Ataei, F., Baccarini, A., Bertozzi, B., Bianchi, F., Brilke, S., Caudillo, L., Chen, D., Chiu, R., Chu, B., Dias, A., Ding, A., Dommen, J., Duplissy, J., Haddad, I. E., Carracedo, L. G., Granzin, M., 480 Hansel, A., Heinritzi, M., Hofbauer, V., Junninen, H., Kangasluoma, J., Kempainen, D., Kim, C., Kong, W., Krechmer, J. E., Kvashin, A., Laitinen, T., Lamkaddam, H., Lee, C. P., Lehtipalo, K., Leiminger, M., Li, Z., Makhmutov, V., Manninen, H. E., Marie, G., Marten, R., Mathot, S., Mauldin, R. L., Mentler, B., Moehler, O., Mueller, T., Nie, W., Onnela, A., Petaja, T., Pfeifer, J., Philippov, M., Ranjithkumar, A., Saiz-Lopez, A., Salma, I., Scholz, W., Schuchmann, S., Schulze, B., Steiner, G., Stozhkov, Y., Tauber, C., Tome, A., Thakur, R. C., Vaisanen, O., Vazquez-Pufleau, M., Wagner, A. C., 485 Wang, Y., Weber, S. K., Winkler, P. M., Wu, Y., Xiao, M., Yan, C., Ye, Q., Ylisirnio, A., Zauner-Wieczorek, M., Zha, Q., Zhou, P., Flagan, R. C., Curtius, J., Baltensperger, U., Kulmala, M., Kerminen, V.-M., Kurten, T., Donahue, N. M., Volkamer, R., Kirkby, J., Worsnop, D. R. and Sipila, M.: Role of iodine oxoacids in atmospheric aerosol nucleation, *Science*, 371, 589–595, <http://doi.org/10.1126/science.abe0298>, 2021.
- Hodshire, A. L., Campuzano-Jost, P., Kodros, J. K., Croft, B., Nault, B. A., Schroder, J. C., Jimenez, J. L. and Pierce, J. R.: 490 The potential role of methanesulfonic acid (MSA) in aerosol formation and growth and the associated radiative forcings, *Atmos. Chem. Phys.*, 19, 3137–3160, <http://doi.org/10.5194/acp-19-3137-2019>, 2019.
- Hoffmann, E. H., Tilgner, A., Schr dner, R., Br uer, P., Wolke, R. and Herrmann, H.: An advanced modeling study on the impacts and atmospheric implications of multiphase dimethyl sulfide chemistry, *Proc. Natl. Acad. Sci. U. S. A.*, 113, 11776–11781, <http://doi.org/10.1073/pnas.1606320113>, 2016.
- 495 Holzer, C., Franzke, Y. J. and Pausch, A.: Current density functional framework for spin–orbit coupling, *J. Chem. Phys.*, 157, 204102, <http://doi.org/doi.org/10.1063/5.0122394>, 2022.
- Kube ka, J., Neefjes, I., Besel, V., Qiao, F., Xie, H.-B. and Elm, J.: Atmospheric Sulfuric Acid-Multi-Base New Particle Formation Revealed through Quantum Chemistry Enhanced by Machine Learning, *J. Phys. Chem. A*, 127, 2091–2103, <http://doi.org/10.1021/acs.jpca.3c00068>, 2023.
- 500 Kuhn, M. and Weigend, F.: Two-component hybrid time-dependent density functional theory within the Tamm-Dancoff approximation, *J. Chem. Phys.*, 142, 034116, <http://doi.org/10.1063/1.4905829>, 2015.
- Kulmala, M., Kontkanen, J., Junninen, H., Lehtipalo, K., Manninen, H. E., Nieminen, T., Pet j , T., Sipil , M., Schobesberger, S., Rantala, P., Franchin, A., Jokinen, T., J rvinen, E.,  ijal , M., Kangasluoma, J., Hakala, J., Aalto, P. P., Paasonen, P., Mikkil , J., Vanhanen, J., Aalto, J., Hakola, H., Makkonen, U., Ruuskanen, T., Mauldin, R. L., 3rd, Duplissy, J., Vehkam ki, 505 H., B ck, J., Kortelainen, A., Riipinen, I., Kurt n, T., Johnston, M. V., Smith, J. N., Ehn, M., Mentel, T. F., Lehtinen, K. E., Laaksonen, A., Kerminen, V. M. and Worsnop, D. R.: Direct observations of atmospheric aerosol nucleation, *Science*, 339, 943–946, <http://doi.org/10.1126/science.1227385>, 2013.

- Lehtinen, K. E. J., Dal Maso, M., Kulmala, M. and Kerminen, V.-M.: Estimating nucleation rates from apparent particle formation rates and vice versa: Revised formulation of the Kerminen–Kulmala equation, *J. Aerosol Sci.*, 38, 988–994, 510 <http://doi.org/10.1016/j.jaerosci.2007.06.009>, 2007.
- Lehtipalo, K., Rondo, L., Kontkanen, J., Schobesberger, S., Jokinen, T., Sarnela, N., Kürten, A., Ehrhart, S., Franchin, A., Nieminen, T., Riccobono, F., Sipilä, M., Yli-Juuti, T., Duplissy, J., Adamov, A., Ahlm, L., Almeida, J., Amorim, A., Bianchi, F., Breitenlechner, M., Dommen, J., Downard, A. J., Dunne, E. M., Flagan, R. C., Guida, R., Hakala, J., Hansel, A., Jud, W., Kangasluoma, J., Kerminen, V.-M., Keskinen, H., Kim, J., Kirkby, J., Kupc, A., Kupiainen-Määttä, O., 515 Laaksonen, A., Lawler, M. J., Leiminger, M., Mathot, S., Olenius, T., Ortega, I. K., Onnela, A., Petäjä, T., Praplan, A., Rissanen, M. P., Ruuskanen, T., Santos, F. D., Schallhart, S., Schnitzhofer, R., Simon, M., Smith, J. N., Tröstl, J., Tsagkogeorgas, G., Tomé, A., Vaattovaara, P., Vehkamäki, H., Vrtala, A. E., Wagner, P. E., Williamson, C., Wimmer, D., Winkler, P. M., Virtanen, A., Donahue, N. M., Carslaw, K. S., Baltensperger, U., Riipinen, I., Curtius, J., Worsnop, D. R. and Kulmala, M.: The effect of acid–base clustering and ions on the growth of atmospheric nano-particles, *Nat. Commun.*, 520 7, 11594, <http://doi.org/10.1038/ncomms11594>, 2016.
- Li, J., Ning, A., Liu, L. and Zhang, X.: Atmospheric Bases-Enhanced Iodic Acid Nucleation: Altitude-Dependent Characteristics and Molecular Mechanisms, *Environ. Sci. Technol.*, <http://doi.org/10.1021/acs.est.4c06053>, 2024.
- Li, Y., Shen, J., Zhao, B., Cai, R., Wang, S., Gao, Y., Shrivastava, M., Gao, D., Zheng, J., Kulmala, M. and Jiang, J.: A dynamic parameterization of sulfuric acid–dimethylamine nucleation and its application in three-dimensional modeling, 525 *Atmos. Chem. Phys.*, 23, 8789–8804, <http://doi.org/10.5194/acp-23-8789-2023>, 2023.
- Liakos, D. G., Guo, Y. and Neese, F.: Comprehensive Benchmark Results for the Domain Based Local Pair Natural Orbital Coupled Cluster Method (DLPNO-CCSD(T)) for Closed- and Open-Shell Systems, *J. Phys. Chem. A*, 124, 90–100, <http://doi.org/10.1021/acs.jpca.9b05734>, 2020.
- Liu, L., Li, S., Zu, H. and Zhang, X.: Unexpectedly significant stabilizing mechanism of iodic acid on iodic acid nucleation under different atmospheric conditions, *Sci. Total Environ.*, 859, 159832, <http://doi.org/10.1016/j.scitotenv.2022.159832>, 530 2023.
- Liu, Y., Xie, H.-B., Ma, F., Chen, J. and Elm, J.: Amine-enhanced methanesulfonic acid-driven nucleation: Predictive model and cluster formation mechanism, *Environ. Sci. Technol.*, 56, 7751–7760, <http://doi.org/10.1021/acs.est.2c01639>, 2022.
- Lu, T. and Chen, F.: Multiwfn: a multifunctional wavefunction analyzer, *J. Comput. Chem.*, 33, 580–592, 535 <http://doi.org/10.1002/jcc.22885>, 2012.
- Lu, T. and Chen, Q.: Shermo: A general code for calculating molecular thermochemistry properties, *Comput. Theor. Chem.*, 1200, 113249, <http://doi.org/10.1016/j.comptc.2021.113249>, 2021.
- Ma, F., Xie, H. B., Zhang, R., Su, L., Jiang, Q., Tang, W., Chen, J., Engsvang, M., Elm, J. and He, X. C.: Enhancement of atmospheric nucleation precursors on iodic acid-induced nucleation: Predictive model and mechanism, *Environ. Sci. Technol.*, 57, 6944–6954, <http://doi.org/10.1021/acs.est.3c01034>, 540 2023.

- McGrath, M. J., Olenius, T., Ortega, I. K., Loukonen, V., Paasonen, P., Kurtén, T., Kulmala, M. and Vehkamäki, H.: Atmospheric Cluster Dynamics Code: a flexible method for solution of the birth-death equations, *Atmos. Chem. Phys.*, 12, 2345–2355, <http://doi.org/10.5194/acp-12-2345-2012>, 2012.
- 545 Mohd Zaki, N. H., Ali, A. M. M., Mohamad Taib, M. F., Wan Ismail, W. I. N., Sepeai, S. and Ramli, A.: Dispersion-correction density functional theory (DFT+D) and spin-orbit coupling (SOC) method into the structural, electronic, optical and mechanical properties of  $\text{CH}_3\text{NH}_3\text{PbI}_3$ , *Comput. Condens. Matte.*, 34, e00777, <http://doi.org/10.1016/j.cocom.2022.e00777>, 2023.
- 550 Myllys, N., Kubečka, J., Besel, V., Alfaouri, D., Olenius, T., Smith, J. N. and Passananti, M.: Role of base strength, cluster structure and charge in sulfuric-acid-driven particle formation, *Atmos. Chem. Phys.*, 19, 9753–9768, <http://doi.org/10.5194/acp-19-9753-2019>, 2019.
- Neese, F.: The ORCA program system, *WIREs Comput. Mol. Sci.*, 2, 73–78, <http://doi.org/10.1002/wcms.81>, 2012.
- Ning, A., Liu, L., Ji, L. and Zhang, X.: Molecular-level nucleation mechanism of iodic acid and methanesulfonic acid, *Atmos. Chem. Phys.*, 22, 6103–6114, <http://doi.org/10.5194/acp-22-6103-2022>, 2022a.
- 555 Ning, A., Liu, L., Zhang, S., Yu, F., Du, L., Ge, M. and Zhang, X.: The critical role of dimethylamine in the rapid formation of iodic acid particles in marine areas, *npj Clim. Atmos. Sci.*, 5, 92, <http://doi.org/10.1038/s41612-022-00316-9>, 2022b.
- Ning, A., Shen, J., Zhao, B., Wang, S., Cai, R., Jiang, J., Yan, C., Fu, X., Zhang, Y., Li, J., Ouyang, D., Sun, Y., Saiz-Lopez, A., Francisco, J. S. and Zhang, X.: Overlooked significance of iodic acid in new particle formation in the continental atmosphere, *Proc. Natl. Acad. Sci. U. S. A.*, 121, e2404595121, <http://doi.org/10.1073/pnas.2404595121>, 2024.
- 560 Ning, A. and Zhang, X.: The synergistic effects of methanesulfonic acid (MSA) and methanesulfinic acid (MSIA) on marine new particle formation, *Atmos. Environ.*, 269, 118826, <http://doi.org/10.1016/j.atmosenv.2021.118826>, 2022.
- O'Dowd, C. D. and Leeuw, G. d.: Marine aerosol production: a review of the current knowledge, *Philos. T. R. Soc. A* 365, 1753–1774, <http://doi.org/10.1098/rsta.2007.2043>, 2007.
- 565 Perraud, V., Home, J. R., Martinez, A. S., Kalinowski, J., Meinardi, S., Dawson, M. L., Wingen, L. M., Dabdub, D., Blake, D. R., Gerber, R. B. and Finlayson-Pitts, B. J.: The future of airborne sulfur-containing particles in the absence of fossil fuel sulfur dioxide emissions, *Proc. Natl. Acad. Sci. U. S. A.*, 112, 13514–13519, <http://doi.org/10.1073/pnas.1510743112>, 2015.
- Peterson, K. A., Figgen, D., Goll, E., Stoll, H. and Dolg, M.: Systematically convergent basis sets with relativistic pseudopotentials. II. Small-core pseudopotentials and correlation consistent basis sets for the post-d group 16–18 elements, *J. Chem. Phys.*, 119, 11113–11123, <http://doi.org/10.1063/1.1622924>, 2003.
- 570 Quéléver, L. L. J., Dada, L., Asmi, E., Lampilahti, J., Chan, T., Ferrara, J. E., Copes, G. E., Pérez-Fogwill, G., Barreira, L., Aurela, M., Worsnop, D. R., Jokinen, T. and Sipilä, M.: Investigation of new particle formation mechanisms and aerosol processes at Marambio Station, Antarctic Peninsula, *Atmos. Chem. Phys.*, 22, 8417–8437, <http://doi.org/10.5194/acp-22-8417-2022>, 2022.

- 575 Rong, H., Liu, J., Zhang, Y., Du, L., Zhang, X. and Li, Z.: Nucleation mechanisms of iodic acid in clean and polluted coastal regions, *Chemosphere*, 253, 126743, <http://doi.org/10.1016/j.chemosphere.2020.126743>, 2020.
- Salignat, R., Rissanen, M., Iyer, S., Baray, J.-L., Tulet, P., Metzger, J.-M., Brioude, J., Sellegri, K. and Rose, C.: Measurement report: Insights into the chemical composition and origin of molecular clusters and potential precursor molecules present in the free troposphere over the southern Indian Ocean: observations from the Maïdo Observatory (2150 m a.s.l., Réunion), *Atmos. Chem. Phys.*, 24, 3785–3812, <http://doi.org/10.5194/acp-24-3785-2024>, 2024.
- 580 Sarr, S., Graton, J., Rahali, S., Montavon, G. F. and Galland, N.: Delocalized relativistic effects, from the viewpoint of halogen bonding, *Phys. Chem. Chem. Phys.*, 23, 4064–4074, <http://doi.org/10.1039/D0CP05840H>, 2021.
- Scholz, W., Shen, J., Aliaga, D., Wu, C., Carbone, S., Moreno, I., Zha, Q., Huang, W., Heikkinen, L., Jaffrezo, J. L., Uzu, G., Partoll, E., Leiminger, M., Velarde, F., Laj, P., Ginot, P., Artaxo, P., Wiedensohler, A., Kulmala, M., Mohr, C., Andrade, M., Sinclair, V., Bianchi, F. and Hansel, A.: Measurement report: Long-range transport and the fate of dimethyl sulfide  
585 oxidation products in the free troposphere derived from observations at the high-altitude research station Chacaltaya (5240 m a.s.l.) in the Bolivian Andes, *Atmos. Chem. Phys.*, 23, 895–920, <http://doi.org/10.5194/acp-23-895-2023>, 2023.
- Sipilä, M., Sarnela, N., Jokinen, T., Henschel, H., Junninen, H., Kontkanen, J., Richters, S., Kangasluoma, J., Franchin, A., peräkylä, O., Rissanen, M. P., Ehn, M., Vehkamäki, H., Kurten, T., Berndt, T., Petäjä, T., Worsnop, D., Ceburnis, D., Kerminen, V. M., Kulmala, M. and O'Dowd, C.: Molecular-scale evidence of aerosol particle formation via sequential  
590 addition of HIO<sub>3</sub>, *Nature*, 537, 532–534, <http://doi.org/10.1038/nature19314>, 2016.
- Stolzenburg, D., Simon, M., Ranjithkumar, A., Kürten, A., Lehtipalo, K., Gordon, H., Ehrhart, S., Finkenzeller, H., Pichelstorfer, L., Nieminen, T., He, X.-C., Brilke, S., Xiao, M., Amorim, A., Baalbaki, R., Baccarini, A., Beck, L., Bräkling, S., Caudillo Murillo, L., Chen, D., Chu, B., Dada, L., Dias, A., Dommen, J., Duplissy, J., El Haddad, I., Fischer, L., Gonzalez Carracedo, L., Heinritzi, M., Kim, C., Koenig, T. K., Kong, W., Lamkaddam, H., Lee, C. P., Leiminger, M., Li,  
595 Z., Makhmutov, V., Manninen, H. E., Marie, G., Marten, R., Müller, T., Nie, W., Partoll, E., Petäjä, T., Pfeifer, J., Philippov, M., Rissanen, M. P., Rörup, B., Schobesberger, S., Schuchmann, S., Shen, J., Sipilä, M., Steiner, G., Stozhkov, Y., Tauber, C., Tham, Y. J., Tomé, A., Vazquez-Pufleau, M., Wagner, A. C., Wang, M., Wang, Y., Weber, S. K., Wimmer, D., Wlasits, P. J., Wu, Y., Ye, Q., Zauner-Wieczorek, M., Baltensperger, U., Carslaw, K. S., Curtius, J., Donahue, N. M., Flagan, R. C., Hansel, A., Kulmala, M., Lelieveld, J., Volkamer, R., Kirkby, J. and Winkler, P. M.: Enhanced growth rate of  
600 atmospheric particles from sulfuric acid, *Atmos. Chem. Phys.*, 20, 7359–7372, <http://doi.org/10.5194/acp-20-7359-2020>, 2020.
- Takashima, H., Kanaya, Y., Kato, S., Friedrich, M. M., Van Roozendaal, M., Taketani, F., Miyakawa, T., Komazaki, Y., Cuevas, C. A., Saiz-Lopez, A. and Sekiya, T.: Full latitudinal marine atmospheric measurements of iodine monoxide, *Atmos. Chem. Phys.*, 22, 4005–4018, <http://doi.org/10.5194/acp-22-4005-2022>, 2022.
- 605 Verstraete, M. J., Torrent, M., Jollet, F. c., Zérah, G. and Gonze, X.: Density functional perturbation theory with spin-orbit coupling: Phonon band structure of lead, *Phys. Rev. B*, 78, 045119, <http://doi.org/10.1103/PhysRevB.78.045119>, 2008.

- Xavier, C., de Jonge, R. W., Jokinen, T., Beck, L., Sipila, M., Olenius, T. and Roldin, P.: Role of Iodine-Assisted Aerosol Particle Formation in Antarctica, *Environ. Sci. Technol.*, 58, 7314–7324, <http://doi.org/10.1021/acs.est.3c09103>, 2024.
- 610 Xia, D., Chen, J., Yu, H., Xie, H. B., Wang, Y., Wang, Z., Xu, T. and Allen, D. T.: Formation Mechanisms of Iodine-Ammonia Clusters in Polluted Coastal Areas Unveiled by Thermodynamics and Kinetic Simulations, *Environ. Sci. Technol.*, 54, 9235–9242, <http://doi.org/10.1021/acs.est.9b07476>, 2020.
- Yan, J., Jung, J., Zhang, M., Xu, S., Lin, Q., Zhao, S. and Chen, L.: Significant Underestimation of Gaseous Methanesulfonic Acid (MSA) over Southern Ocean, *Environ. Sci. Technol.*, 53, 13064–13070, <http://doi.org/10.1021/acs.est.9b05362>, 2019.
- 615 Yu, F. and Luo, G.: Modeling of gaseous methylamines in the global atmosphere: impacts of oxidation and aerosol uptake, *Atmos. Chem. Phys.*, 14, 12455–12464, <http://doi.org/10.5194/acp-14-12455-2014>, 2014.
- Zhang, R., Khalizov, A., Wang, L., Hu, M. and Xu, W.: Nucleation and growth of nanoparticles in the atmosphere, *Chem. Rev.*, 112, 1957–2011, <http://doi.org/10.1021/cr2001756>, 2012.
- Zhang, R., Xie, H. B., Ma, F., Chen, J., Iyer, S., Simon, M., Heinritzi, M., Shen, J., Tham, Y. J., Kurtén, T., Worsnop, D. R., Kirkby, J., Curtius, J., Sipilä, M., Kulmala, M. and He, X. C.: Critical Role of Iodous Acid in Neutral Iodine Oxoacid  
620 Nucleation, *Environ. Sci. Technol.*, 56, 14166–14177, <http://doi.org/10.1021/acs.est.2c04328>, 2022.